Appl Nanosci (2014) 4:719–732
DOI 10.1007/s13204-013-0244-7

ORIGINAL ARTICLE

Gas sensing of Au/n-SnO_2/p-PSi/c-Si heterojunction devices prepared by rapid thermal oxidation

Marwa Abdul Muhsien · Evan T. Salem · Ibrahim R. Agool · Haidar Hamed Hamdan

Received: 27 April 2013 / Accepted: 1 June 2013 / Published online: 3 July 2013
© The Author(s) 2013. This article is published with open access at Springerlink.com

Abstract Transparent and conducting SnO_2 thin film has been produced on (quartz, ITO, silicon and porous silicon) substrates using rapid photothermal oxidation of pure Sn in air at 600 °C oxidation temperature and different oxidation time. The structural, optical, electrical properties, scan electron microscope and atomic force microscope of the prepared films were studied. The transmittance T in the visible and NIR was investigated; the allowed direct energy gap was determined to be 3.18 eV at optimum condition of 600 °C and 90 s. The dependence of the resistivity on the film thickness and oxidation time has been studied. The optimum thickness of high transmittance and lowest resistivity is about 150 nm for SnO_2, where $\rho = 1.7 \times 10^{-3}$ Ω cm and $T = 88$ %. The sensitivity behaviors of the n-SnO_2/p-PSi/c-Si-based gas sensor to H_2 and CO_2 gas were investigated. The film sensitivity dependence on the temperature and test gas concentration was tested and the optimum operation temperature was determined at around 250 and 300 °C with an applied voltage was constant at 2.5 V.

Keywords Tin oxide · Rapid thermal oxidation · Thin films · Atomic force microscope · n-SnO_2/p-PSi/c-Si gas sensor · SEM

Introduction

When a polycrystalline tin oxide (SnO_2) semiconductor thin film is exposed to air, physisorbed oxygen molecules pick up electrons from the conduction band of SnO_2 and change to $O^-_{2(ads)}$ or $O^-_{(ads)}$ species (Seal and Shukla 2002). Consequently, a positive space-charge layer forms just below the surface of SnO_2 particles, which creates a potential barrier between the particles increasing the electrical resistance of the SnO_2 film. However, when a reducing gas comes in contact with the film, it gets oxidized via reaction with the $O^-_{2(ads)}$ or $O^-_{(ads)}$ species and subsequently electrons are reintroduced into the electron depletion layer, leading to decrease in the potential barrier. The sensitivity of the SnO_2 thin film is usually determined by the ratio $(Ra - Rg)/Rg$ (or Ra/Rg), where Ra and Rg are the resistances of the sensor in air and reducing gas, respectively. SnO_2-based gas sensor has been synthesized in various forms such as thin (Park and Mackenzie 1996; Sakai et al. 2001; Baik et al. 2000; Choi et al. 1997; Song et al. 1998; Cha et al. 1994; Sberveglieri et al. 1992; Michel et al. 1998; Malyshev et al. 1992) or thick films (Mishra and Agarwal 1994; Devi et al. 1999; Shimizu et al. 1993; Katsuki and Fukui 1998) and pellets (Jayaraman et al. 1999; Chaudhary et al. 1998, 1999). Thin films are synthesized using sols, which are prepared using either alkoxide (Park and Mackenzie 1996) or chloride (Sakai et al. 2001) precursors utilizing either dip (Park and Mackenzie 1996) or spin (Sakai et al. 2001) coating methods. Synthesis of SnO_2 thin films using

M. A. Muhsien (✉) · I. R. Agool
Department of Physics, College of Science, Al-Mustansiriyah University, Baghdad, Iraq
e-mail: marwa_alganaby@yahoo.com

E. T. Salem
Laser and Optoelectronic Branch, School of Applied Sciences, University of Technology, Baghdad, Iraq

H. H. Hamdan
Department of Physics, College of Science, Baghdad University, Baghdad, Iraq

hydrothermally treated sol (Sakai et al. 2001; Baik et al. 2000) and other conventional techniques such as ion-assisted deposition (Choi et al. 1997; Song et al. 1998), sputtering (Cha et al. 1994; Malyshev et al. 1992), evaporation (Carbajal et al. 2000), chemical vapor deposition (Brown et al. 2000), spray pyrolysis (Niranjan et al. 2002) have been reported. On the other hand, thick films are processed using a paste (Mishra and Agarwal 1994; Devi et al. 1999; Shimizu et al. 1993; Katsuki and Fukui 1998) prepared by mixing SnO_2 powder and a binder in a suitable solvent such as water or acetone, which is then applied using screen printing technology (Mishra and Agarwal 1994) on a suitable substrate. Mixing SnO_2 powder with polyvinyl alcohol (PVA) polymer and then pressing the mixed powders into a pellet, which is subsequently sintered at higher temperature, forms pellets (Jayaraman et al. 1999; Chaudhary et al. 1998, 1999). However, a lack of consistency in the sensor properties has been a major problem associated with all these techniques. The processing of SnO_2 semiconductor gas sensor based on pellets or thick film technology are practically excluded from integration in the fabrication of intelligent microsystems, not only due to processing incompatibility but also due to the high power consumption for the gas-sensing applications. Thin film technology based on physical methods like vacuum evaporation or sputtering for SnO_2 deposition, combined with ion-implantation for doping the films with metal ions, is very expensive and may suffer composition inhomogeneity and poor capability to provide good step coverage for topographies with very high aspect ratios. On the other hand, it is well known that the sol–gel technique (used for thin films) has several advantages such as easy control of film thickness, low-cost processing, and ability to produce ultrafine particles, and to coat large complex shapes (Klein 1988). The gas-sensing properties of SnO_2 semiconductor thin film has been found to depend strongly on the method of processing. Among the structural parameters, the nanocrystallite size (Seal and Shukla 2002) and the film thickness (Park and Mackenzie 1996) have pronounced effect on the gas sensitivity. It is now recognized that SnO_2 semiconductor thin film can have maximum gas sensitivity only if the nanocrystallite size within the film is comparable with its space-charge layer thickness (Seal and Shukla 2002). Hence, the major objectives of the present investigation are set to synthesize SnO semiconductor thin film, having nanosized crystallites (critical parameters for achieving maximum sensitivity) using the rapid thermal oxidation technique. Various analytical techniques such as scanning electron microscopy (SEM), X-ray diffraction (XRD), atomic force microscopy (AFM) and optical properties are utilized in the present investigation. Besides, the present study also focuses on demonstrating the suitability of such SnO_2/PSi/c-Si device for sensing H_2, CO_2 gas.

Experimental work

High purity of tin (Sn) thin film was deposited on (quartz, ITO glass, p-type silicon and p-type PSi single crystal (111) silicon substrates) using thermal evaporation technique at room temperature under a vacuum pressure of 10^{-6} Torr. Electrochemical anodization was performed in dark to produce porous Si layers on polished p-type, single crystal (111) oriented Si wafers with a resistivity of 0.01–0.02 Ω cm and a thickness of $\sim 508 \pm 5$ µm, using a 1:4 mixture of 48 % HF: 98 % ethanol as an electrolyte. Initially, the Si wafers were cleaned successively in a sonicating bath with CCl_4, toluene, acetone, ethyl alcohol and 18.5 M cm deionized water. The anodization was carried out with the distance between the Si substrate to the Pt counter electrode fixed at ~ 2.5 cm, using a current density of 40 mA/cm^2 for a fixed time of 5 min. The wafer and platinum cathode were placed in a Teflon jig, schematically illustrated in Fig. 1a. The surfaces of Si substrate and Pt cathode were kept parallel to each other and the current flow in the etchant was normal to the wafer surface. After the anodization, the PSi layers were dried in the following way to reduce the capillary stress using pentane, which has very low surface tension and no chemical reactivity with the PSi layer. The samples were rinsed first with pentane, then with 98 % methanol and finally with deionized water (18.5 M cm). Next, the samples were dried at about 60 °C on a hot plate rather than drying in the N_2 nozzle to avoid cracking and peeling of the PSi layer.

The resistivity and type of conductivity of the Si substrates were measured using four-point probe (FPP) technique. SnO_2 film was obtained with the aid of rapid photo-thermal oxidation system with halogen lamp as oxidation source. The oxidation condition used to form SnO_2 film was 600 °C and different oxidation times. Figure 1b shows the system used to prepare the oxide film; where a quartz tube of 3 cm diameter with two open ends was used to ensure the flow of air through it. The source of dry oxygen was used. 650-W halogen lamps were used to provide light and heat radiation and a variable power supply to control the output power. A k-type thermocouple was used to monitor samples temperature. The silicon sample was used as substrate for TCO's/PSi heterojunction. Ohmic contacts were fabricated by evaporating 99.999 purity aluminum wires for back contact, and 99.999 pure gold were used as front contact through special mask using Edwards coating system. A boat of tungsten was used to include the evaporated source. Figure 1c illustrates two 8- and 10-finger interdigitated electrode IDE metal masks which were utilized in this work. The samples were fixed in the evaporation system.

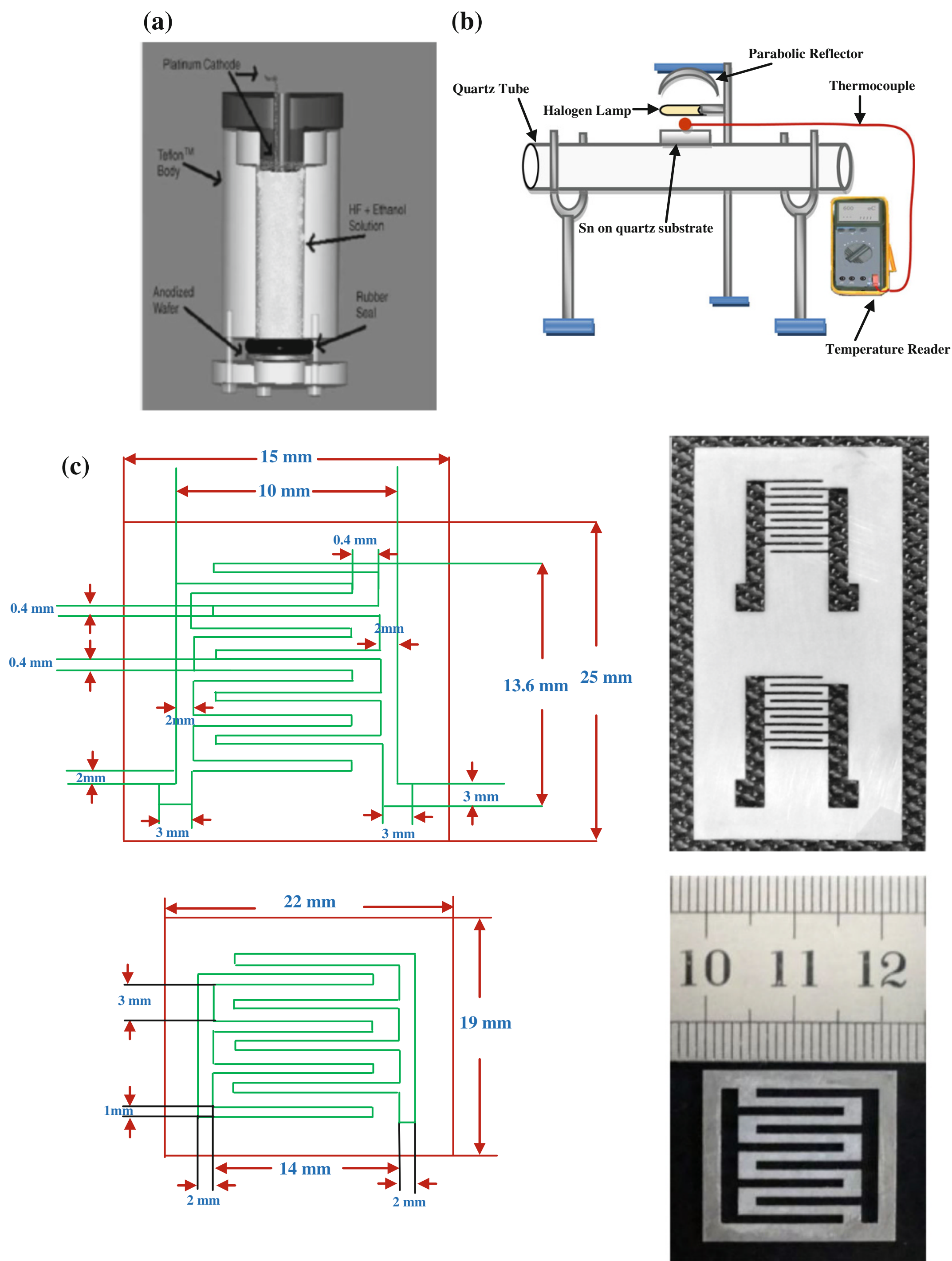

Fig. 1 **a** Schematic illustration of the porous silicon etching setup and **b** rapid photo-thermal oxidation (RTO) setup and **c** a schematic diagram of the IDE masks utilized in this work

Results and discussion

XRD-diffraction

The structure and lattice parameters of SnO_2 films were analyzed by a LabX XRD 6000 SHIMADZU XR-diffractometer with Cu Kα radiation of (voltage 30 kV, current 15 mA, scanning speed = 4°/min). Figure 2 shows the diffraction pattern for samples prepared at oxidation temperature 600 °C and different oxidation time. The XRD patterns at oxidation time of 60 s are shown in Fig. 2a. It shows that the peaks appeared at $2\theta = 33.8436°$ and

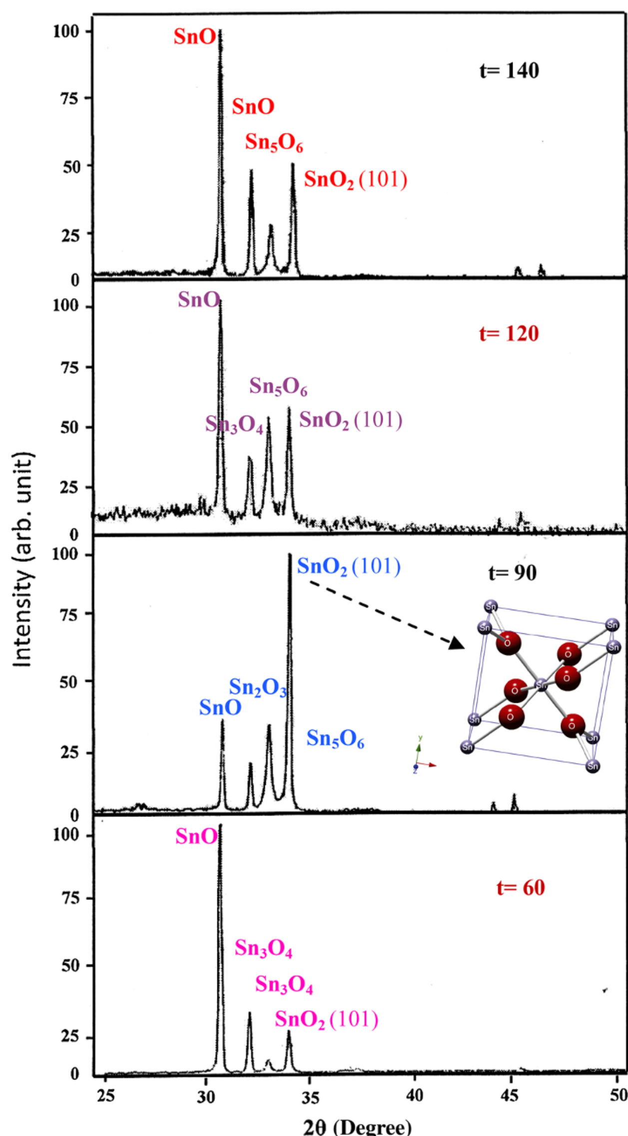

Fig. 2 X-Ray diffraction patterns for SnO_2 thin films prepared at different oxidation time and 600 °C

$2\theta = 34.0896°$ are corresponding to the diffraction from (101) planes which are related to the formation of SnO_2 films. At 90 s oxidation time and 600 °C oxidation temperature, Fig. 2b shows that the structures of films are clearly improved where a significant increase in peak intensity at (101) plane can be attributed to the improvement in the structural order, which can also be attributed to the increase in the SnO_2 film density, resulting in the demonstration of the (101) SnO_2 peak rather than the other peak. This indicates the formation of nearly stoichiometry SnO_2 films. The intensities of these peaks reduce with the increasing of oxidation time up to 120 s as shown in Fig. 2c. The results below ensure that the optimum value of oxidation temperature is 600 °C and oxidation time is 90 s. The deviation in XRD peak of the film with respect to the standard ASTM data is attributed to the mechanical microstress produced by different sources like impurities, defects and vacancies reside in the film structure. Results at higher oxidation time 140 s and at the same oxidation temperature are shown in Fig. 2d, which recognizes the peaks at $2\theta = 33.9813°$ in the spectra of SnO_2 film corresponding to the reflection from (101) plane. The presence of sharp peak (in all deprogram) indicates that all films are polycrystalline in nature with a tetragonal structure and in accordance with data reported in literature (Gordillo et al. 1994; Choe et al. 1999; Mitchell 2004). Table 1 shows the effect of oxidation times on the XRD characteristics evaluated from the diffrograms. In the case of tetragonal structure which is the ruling form for SnO_2 thin films, the lattice constants are $a = b \neq c$ as shown in Table 2. These constants change with structural change caused by the different parameters such as deposition technique, doping, substrate, etc., and the lattice constant can be found by measuring different values of *(d)* not less than two or three or four times of X-ray spectrum using the formula (Mosadegh Sedghi and Vesali Naseh 2009):

$$\frac{1}{d^2} = \frac{(h^2 + k^2)}{a^2} + \frac{l^2}{c^2} \quad (1)$$

where h, k, l are the Miller indices of the lattice plane. The values of lattice constants for SnO_2 films prepared at different oxidation temperature and oxidation time have been listed in Table 2. The grain size (D) is calculated using the Scherrer formula from the full-width half-maximum (FWHM) (β) (Van and Dinh 1998):

$$D = \frac{K\lambda}{\beta \cos\theta} \quad (2)$$

where λ is the wavelength of the X-ray used, β is the FWHM, D is the grain size value and θ is half the angle between incident and the scattered X-ray beams. The *(D)* values are listed in the Table 3. It shows that grain size of the films is increased with increasing of oxidation time up to (90 s).The intense and sharp peaks in XRD pattern reveal the good crystallinity of the films and also confirm the stoichiometric nature of SnO_2 films.

Scan electron microscope (SEM)

Surface morphologies obtained through SEM study carried out by (Hitachi FE-SEM model S-4160, Japan) in University of Tehran at 15 kV of SnO_2 films prepared at oxidation temperature 600 °C and different oxidation times. SEM micrograph shows that surface of SnO_2 thin films are smoother as shown in Fig. 3a–d. The films consist of small particles distributed on the surface that shows nanostructure properties. The structure is polycrystalline with very fine pores distributed fairly uniformly on the film surface.

Table 1 XRD patterns characteristics of SnO_2 films at various oxidation times

Deposition condition	$(2\theta)°$	I/I_1 XRD	d (Å) XRD	(hkl)	$(2\theta)°$ ASTM	I/I_1 ASTM	d (Å) ASTM	Type
$t = 60$ s	30.8484	100	2.89626	–	30.916	90	2.89	SnO
$T = 600$ °C	32.234	25	2.77486	–	32.315	50	2.768	Sn_3O_4
	33.1044	8	2.70386	–	33.014	50	2.711	Sn_3O_4
	34.0896	10	2.62794	101	34.061	80	2.63	SnO_2
$t = 90$ s	30.7698	31	2.90348	101	30.807	80	2.9	SnO
$T = 600$ °C	32.7901	6	2.72906	30	32.964	30	2.715	Sn_2O_3
	33.0188	30	2.71068	–	33.026	30	2.71	Sn_5O_6
	34.0027	100	2.63446	101	34.061	80	2.63	SnO_2
$t = 120$ s	30.9004	100	2.89151	–	30.916	90	2.89	SnO
$T = 600$ °C	32.3045	26	2.76896	–	32.315	50	2.768	Sn_3O_4
	33.1776	42	2.69806	–	33.026	30	2.71	Sn_5O_6
	34.1664	45	2.62221	101	34.195	80	2.62	SnO_2
$t = 140$ s	30.755	100	2.90485	101	30.807	80	2.9	SnO
$T = 600$ °C	32.1293	40	2.78366	21	32.172	40	2.78	SnO
	33.0054	18	2.71175	–	33.026	30	2.71	Sn_5O_6
	33.9813	46	2.63607	101	33-928	63	2.64	SnO_2

Table 2 Lattice constants as a function of oxidation temperature and oxidation time of SnO_2 thin film

Deposition condition	Investigated line	Type	Lattice (a) (Å)	Lattice (c) (Å)
$t = 60$ s, $T = 600$ °C	101	SnO_2	4.706	3.168
$t = 90$ s, $T = 600$ °C	101	SnO_2	4.717	3.175
$t = 120$ s, $T = 600$ °C	101	SnO_2	4.695	3.161
$t = 140$ s, $T = 600$ °C	101	SnO_2	4.720	3.177
ASTM	101	SnO_2	4.750	3.198

Table 3 Grain size of SnO_2 thin film

Deposition condition	Investigated line	Type	β (degree)	Grain size (D) nm
$t = 60$ s, $T = 600$ °C	101	SnO_2	0.1712	50.7169
$t = 90$ s, $T = 600$ °C	101	SnO_2	0.1544	56.2223
$t = 120$ s, $T = 600$ °C	101	SnO_2	0.1945	44.6505
$t = 140$ s, $T = 600$ °C	101	SnO_2	0.1557	55.7497

We can observe a dense granular structure. The grains have different shapes and sizes. The grain size found using SEM is smaller than those derived from X-ray diffraction. From SEM observations given by Fig. 3, we note that the average grain size is comparable to the film thickness which is <100 nm.

Atomic force microscope (AFM)

It is known that the surface properties of the transparent conducting oxide films influence their optical and electrical properties which are important factors for applications in optoelectronic devices; in principle, the increase in surface roughness of the films leads to a decrease in the efficiency for photovoltaic properties, therefore, it is very important to investigate the surface morphology of the films (Van and Dinh 1998). The AFM technique uses a laterally moving tip, while the cantilever reflects the sample's topography, or the Z measurements. Even though the tip is very sharp, it is impossible to gather the information from the underside of specimen. The spherical particle will be viewed as a bump by the atomic force microscope. To correct the AFM image for this effect some deconvolution techniques are used. The surface morphology of Ag_2O films as observed from the (AFM-AA3000, Angstrom Advanced Inc., USA) micrographs proves that the grains are uniformly distributed within the scanning area ($1{,}000 \times 1{,}000$ nm) with individual columnar grains extending upwards as shown in Fig. 4. The grain size decreases with the oxidation time increases, while the films presented uniformity. Since the size grain decreases in dimension when the film thickness decreases, it suggests that the charge transport is occurring predominantly intra-grain in cases of lower thickness, or equivalent to greater grains, and that there is a preferential charge transport inter-grain in greater thickness samples, where there are more the interface grains, in this kind of microstructure it is usually not dominated by bulk properties but by grain walls, which either act as low conductivity blockades or as high conductivity carrier accumulation regions. This surface characteristic is important for applications such as solar cells, gas sensors and catalysts (Gyogy and Axente 2000; Al-Hardan and Abdulllah 2009). The root mean square (rms) roughness of the film surface roughness was prepared at different conditions as listed in Table 4.

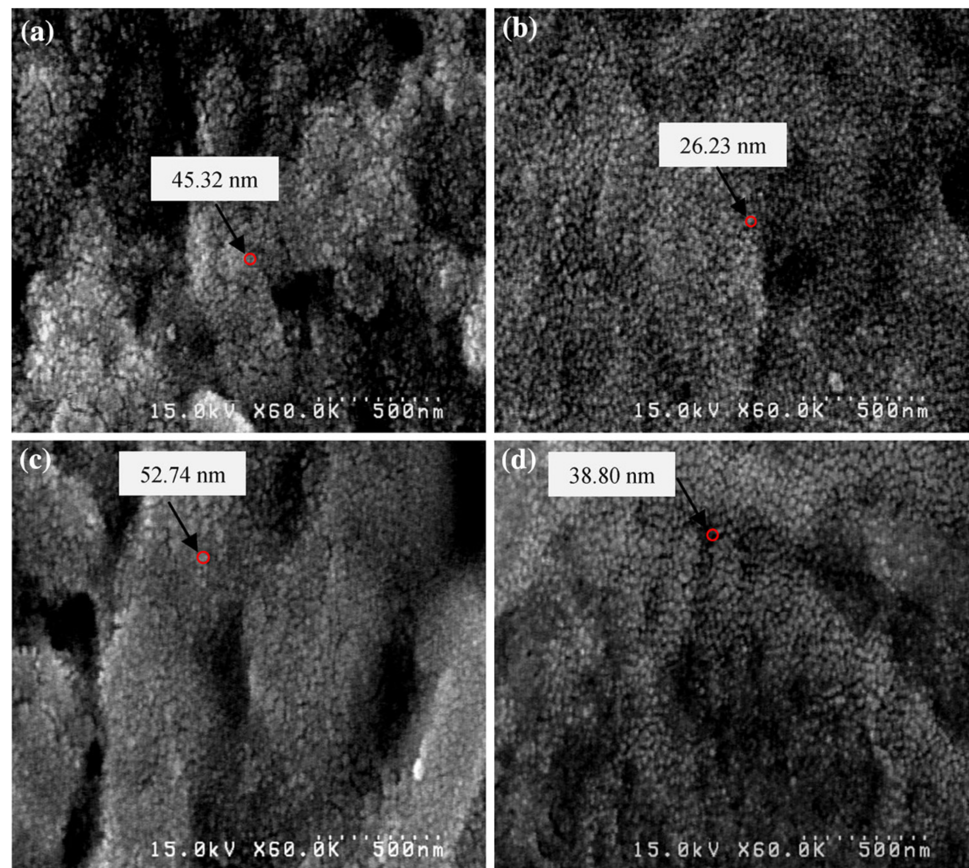

Fig. 3 Scanning electron microscope of SnO_2 film prepared at 600 °C and oxidation time **a** 60 s, **b** 90 s, **c** 120 s and, **d** 140 s

Optical properties

Figure 5 shows the optical transmission (200–1,000) nm as a function of the wavelength for SnO_2 film prepared at different oxidation time and constant oxidation temperature; high transmission (>90 %) was exhibited by films prepared at 120 and 140 s oxidation time, may be because the increase in the oxidation leads to large molecular symmetry (stoichiometry) where (101) SnO_2 films are demonstrated over all other oxide film peaks.

In general, it has been found that the transmission of the films was increased when the oxidation temperature was increased due to film transformation from metal to transparent oxide. The optical band gap was calculated for films prepared at optimum oxidation time and temperature. The band gaps of these films were calculated from Fig. 6 using the formula (Kuku Titilayo 1986):

$$\alpha hv = A(hv - E_g)^m \quad (3)$$

where α = absorption coefficient, h = Planck's constant, υ = frequency of incident light, E_g = band gap of the material, m = factor governing the direct/indirect, etc. transitions of the electrons from the valence band to the conduction band.

The plots of $(\alpha h\upsilon)^2$ against $h\upsilon$ for SnO_2 film prepared at (600 °C) and (90 s) is shown in Fig. 6. The nature of the plot suggests a direct inter-band transition. The extrapolation of the straight-line portion to zero absorption coefficient ($\alpha = 0$) leads to the estimation of band gap energy, this band gap found to be about 3.54 eV. This result is conditional with many other workers (Roman 2006; Yadav et al. 2007; Mohammed Khalid 2005).

The dependences of absorption coefficients α on photon energy are represented in Fig. 7 for the film grown at different oxidation time. The direct optical band gap increases to give a blue shift. This shift is due to increase in carrier concentration which results in filling the bottom of the conduction band and this filling prevents the transition of the photogenerated carriers into the filled levels according to quantum rules and hence leads to far transitions with larger photon energy. This shift is called Burstein–Moss effect. The E_g is found to be about 3.5–3.7 eV at T = 600 °C, and different oxidation times are shown in Fig. 8. These results agree with published literatures (Zhu and Yao 2006).

Electrical properties

The logarithmic conductivity as a function of temperature for SnO_2 oxide samples prepared at the optimum condition is given in Fig. 9. It is clear that the values of conductivity increase with temperature, such as the general

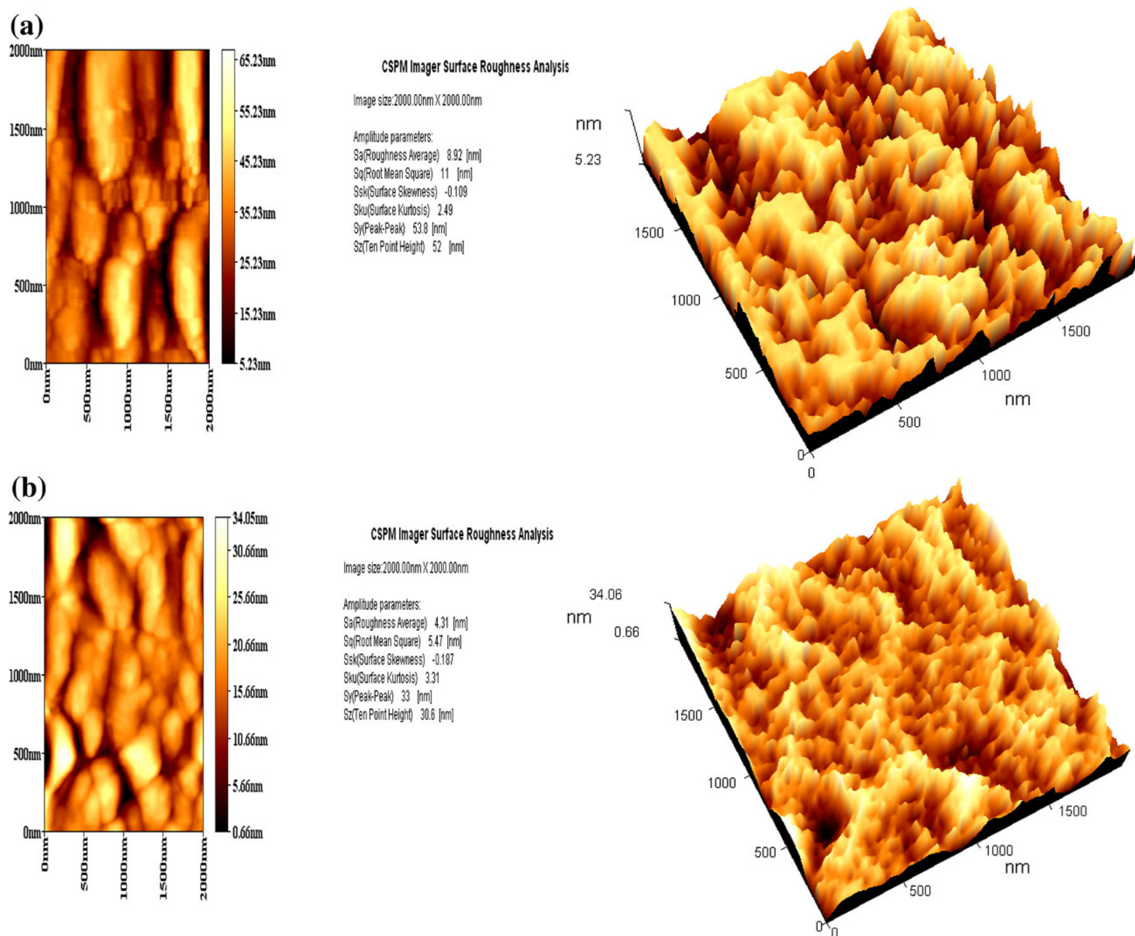

Fig. 4 AFM images of SnO_2 prepared at 600 °C and different oxidation times **a** 60 s, **b** 90 s, **c** 120 s and **d** 140 s

characteristics of the semiconductor with increasing temperature lead to an increase in the number of electron-holes pairs resulting on increased conductivity. The linear proportionality in the curve is related to the increase in the number of ionized carriers from the valance band to the conduction band as the substrate is heated.

The value of the activation energy has been estimated using the following equation (Yoshiaki 2003):

$$\sigma_{dc} = \sigma_o \exp\left(\frac{-E_a}{kT}\right) \quad (4)$$

where σ_o is the high temperature limit of conductivity, E_a is activation energy and kT is the thermal energy associated with temperature variation in the measurement, where k is Boltzman constant and T is absolute temperature (Table 5).

The variation in the resistivity with oxidation times for SnO_2 film is shown in Fig. 10. The decrease in resistivity may be due to the conversion of SnO to SnO_2 so that the SnO concentration is decreased, leading to an increased conductivity due to the filling of the oxygen vacancies in SnO_2 and hence the oxygen-deficient SnO_2 would become nearly stoichiometric and insulating. The minimum resistivity of the SnO_2 films obtained in this work is about $1.7 \times 10^{-3}\ \Omega$ cm, and this agrees with the result in similar work (Gordillo et al. 1994; Raviendra and Sharma 1985).

The conductivity type of SnO_2 films was determined by Hall effects. Table 6 shows that the results indicate that the materials under study are n-type semiconductors possibly due to the donor formation by O_2 vacancies; these results agree with the results of Zhang and Tian (2011).

The carrier concentration and Hall mobility as a function of oxidation times are demonstrated in Fig. 11. The carrier concentration increases up to oxidation time 60 s. The variation of carrier concentrations can ascribe to the generation of conduction electrons and, thus, increasing the carrier concentration. The mobility of SnO_2 films shows a continuous decrease as the increasing of oxidation times. The actual value of mobility is determined by the interaction between the various scattering centers and free carriers. This result in a good agreement with that obtained by Zhang and Tian (2011a, b).

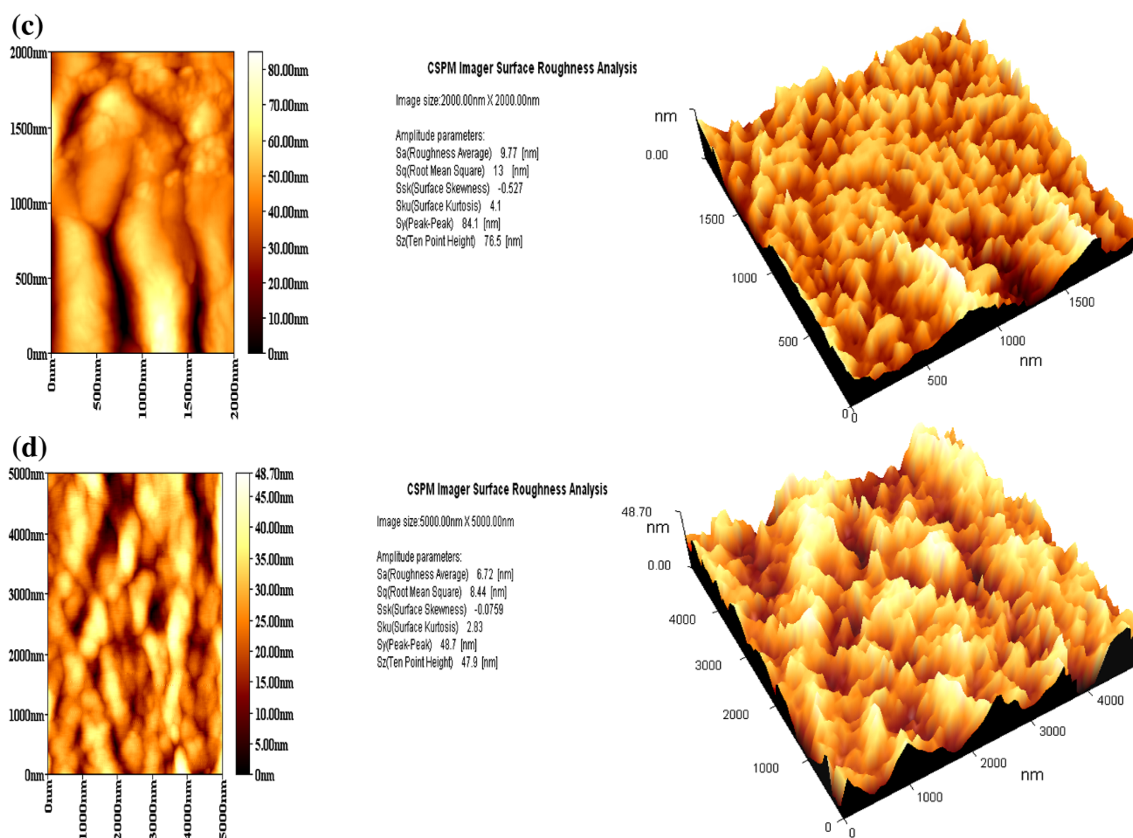

Fig. 4 continued

Table 4 The grain size of SnO_2 film prepared at different oxidation time and oxidation temperature 600 °C

Sample	Grain size (nm)	Sa (roughness average) (nm)	Sq (root mean square) (nm)	Sz (ten point height) (nm)
250 nm, 600 °C and 60 s	51.11	8.92	11	52
250 nm, 600 °C and 90 s	57.74	4.31	5.47	30.6
250 nm, 600 °C and 120 s	45.55	9.77	13	76.5
250 nm, 600 °C and 140 s	56.14	6.72	8.44	47.9

Scan electron microscope (SEM) for porous silicon

The SEM study was carried out by (VEGA TESCAN-SEM) in University of Technology, Baghdad, Iraq at 20 kV. The reproducibility of structural and optical properties of porous silicon is a fundamental issue (Pascual et al. 2002) that helps in device fabrication related to PSi. In this work, we stick to the optimum experimental parameters in respect of the PSi preparation with desired reproducibility. The porosity (gravimetric) values of the PSi layers formed on p-type Si wafers (henceforth, called as p-PSi, respectively) were 85 %, respectively, for an etching time of 5 min using Eq. (3). An estimation of the porosity is obtained gravimetrically: first, the weight of the virgin wafer is measured before anodization (M_1), then after anodization (M_2), and finally after dissolution of the porous silicon layer (M_3) in a 1 M solution of sodium hydroxide (NaOH). After determining these values, the porosity is given by the following equation (Bisi et al. 2000):

$$\text{Porosity}\,\% = \frac{M_1 - M_2}{M_1 - M_3} \tag{5}$$

The etching time has been fixed at 5 min with the current density of 40 mA/cm^2 as an optimum condition, since the reproducibility of porosity values lies within 2–3 %. It is well known that PSi can exist in different microstructural forms depending upon various electrochemical parameters, silicon doping and resistivity (Kocka et al. 1995). According to IUPAC classification of pore size, our PSi samples should belong to either the mesoporous (2–50 nm) or the nanoporous (<2 nm) region

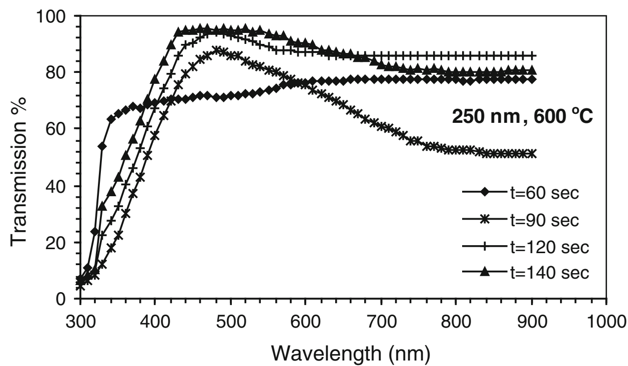

Fig. 5 Optical transmission as a function of wavelength for SnO_2 thin films prepared on quartz substrate different oxidation time

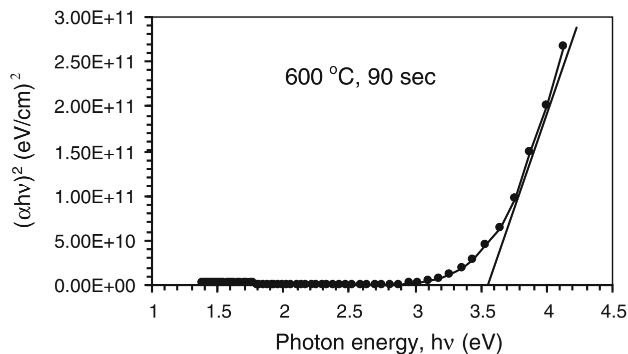

Fig. 6 Energy band gap of the SnO_2 at oxidation temperature (600 °C) and oxidation time (90 s)

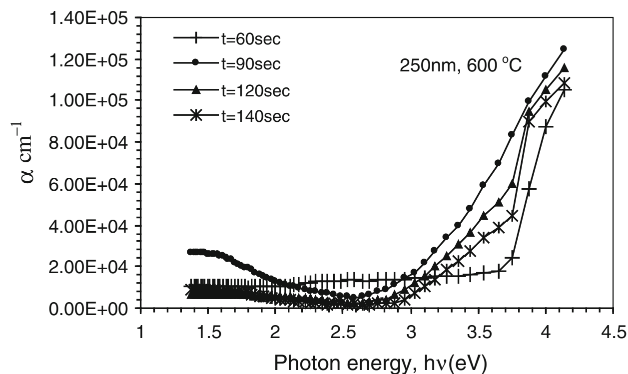

Fig. 7 α (cm^{-1}) vs. $h\upsilon$ of SnO_2 films at different oxidation time

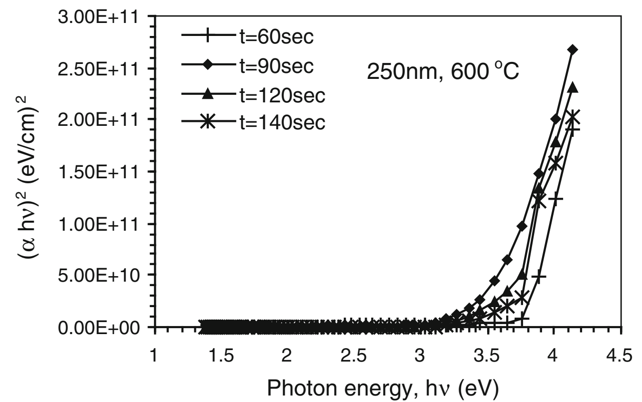

Fig. 8 $(\alpha h\upsilon)^2$ $(eV/cm)^2$ vs. $h\upsilon$ of SnO_2 films at different oxidation time

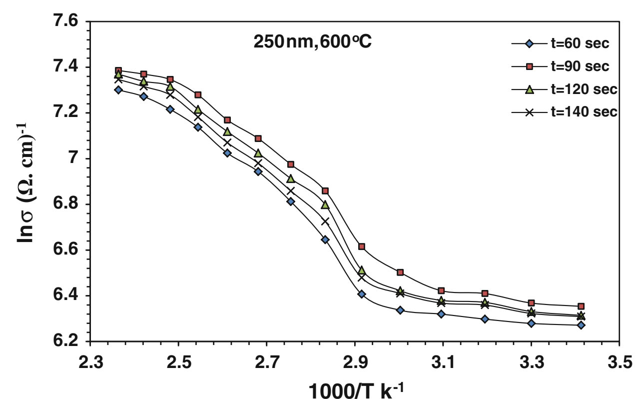

Fig. 9 Electrical conductivity vs. 1,000/T

as evident from the plan-view SEM micrograph (Fig. 12a). As expected, the PSi surface p-type Si wafers are characterized by the presence of large number of pores, more or less, regular in size.

It is established (Gaburro et al. 2000) that the higher thickness of porous silicon poses the danger of a bad electrical contact on the PSi device, resulting in the worst efficiency characteristics, although it helps in improving the power efficiency. The thickness values of the PSi layers formed on p-type Si wafers (henceforth, called as p-PSi, respectively) were 50.78 µm, respectively, for an etching time of 5 min using Eq. (4). The thickness of the layers is another important parameter that is closely related to the etching parameters of anodization time and hydrofluoric acid concentration. Similar to porosity, the thickness can be approximated gravimetrically by the following equation:

$$T_{\mathrm{PSi}} = K * J^m * t \tag{6}$$

where T_{PSi} in (cm), J = etching current density (mA/cm^2), t = etching time (s). Constants K and m are tabulated in Table 7 and depend on HF concentration. Another way to measure the film thickness is by direct determination using the SEM or AFM (Berger et al. 2001).

Figure 12a shows the topography of the porous silicon formed by the electrochemical anodization process of monocrystalline silicon in HF-based solution at 40 mA/cm^2 for 5 min in dark and white at room temperature. As shown, a nearly uniform distribution of pores and a sponge-like structure of the porous layer are obtained. The porosity and thickness of porous silicon is a major concern of researchers in the field. However, understanding how to control PSi morphology is extremely difficult owing to the

Table 5 Activation energy of SnO_2 film prepared at different oxidation time and oxidation temperature 600 °C

Sample	E_a1 (eV) at low temperatures	E_{a2} (eV) at high temperatures
250 nm, 600 °C and 60 s	0.021312	0.086302
250 nm, 600 °C and 90 s	0.0419	0.072398
250 nm, 600 °C and 120 s	0.031085	0.078255
250 nm, 600 °C and 140 s	0.027462	0.084223

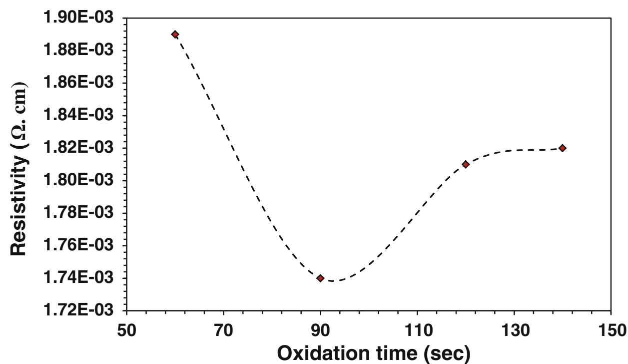

Fig. 10 Resistivity as a function of oxidation times for SnO_2 thin film

Table 6 Hall coefficient of SnO_2 film prepared at different oxidation time and oxidation temperature 600 °C

Sample	R_H (cm^3/°C)	Type
250 nm, 600 °C and 60 s	0.3429	n-type
250 nm, 600 °C and 90 s	0.0497	n-type
250 nm, 600 °C and 120 s	0.0848	n-type
250 nm, 600 °C and 140 s	0.1834	n-type

large number of controlling factors (Gaburro et al. 2000; Berger et al. 2001). The morphology of PSi is also strongly affected by the etching current density. The silicon dissolution process requires the presence of fluorine ions (F^-) and holes (h^+). As shown in Fig. 12b, when the fluorine ions are delivered faster than the holes, the inter-pore regions of PSi are depleted of holes; and further etching occurs only at the pore tips, where the holes are focused by the electric field. When the current density decreases, the number of holes at the pore tips drops, which lead to smaller pore sizes. Thus, the porosity (defined as the percentage of void space in the material) can be precisely controlled by the etching current density.

Atomic force microscope for tin oxide/porous silicon

The surface morphology of as deposited tin thin metal film on the porous silicon substrate before any heat treatment

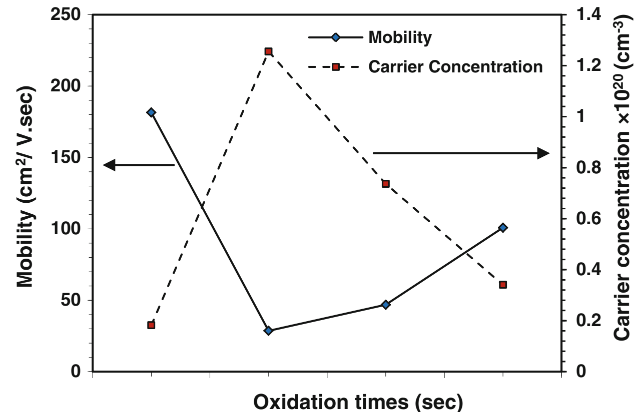

Fig. 11 The variation of carrier concentration and hall mobility with doping concentration of SnO2:Pd films

Table 7 Coefficient determined for the empirical Eq. 7

HF concentration (%)	K (cm^3/mA s)	m
30	1.01×10^{-7}	0.98
40	1.05×10^{-7}	0.96
50	1.13×10^{-7}	0.92

revealed as shown in Fig. 13a, that the poured structure was destroyed; this is related to the thin film growth mechanism.

By rapid thermal oxidation at 600 °C oxidation temperature and 90 s oxidation time (Fig. 13b), a re-crystallization of the deposited atom above the nanocrystalline silicon substrate begins to take place and at the same time the surface morphology of the porous silicon itself changed due to the formation of nano silicon dioxide (SiO_2) and the reduction in porous silicon grain size and roughness. The result shows a uniform net work-like porous surface with a root mean square value (39.1 nm) that revealed low roughnesses of about (30.6 nm) which insure homogeneity in pore size values, comparing with Fig. 13a where the RMS was (33.2 nm) and the roughness about (23.8) the increase in its value on first case related to the re-distribution of oxide atoms on the porous surface and also associated with the increase in the average grain size (from 216.41 to 222.32 nm). The obtained films display smooth, uniform grain size and void free, i.e., very limited no. of droplets was observed.

XRD for tin oxide/porous silicon

XRD is a convenient method to evaluate the degree of crystallinity in PSi, although it is less direct than electron microscopy techniques. Figure 14 shows the XRD pattern of non-etched silicon (fresh silicon); it is clear that just one

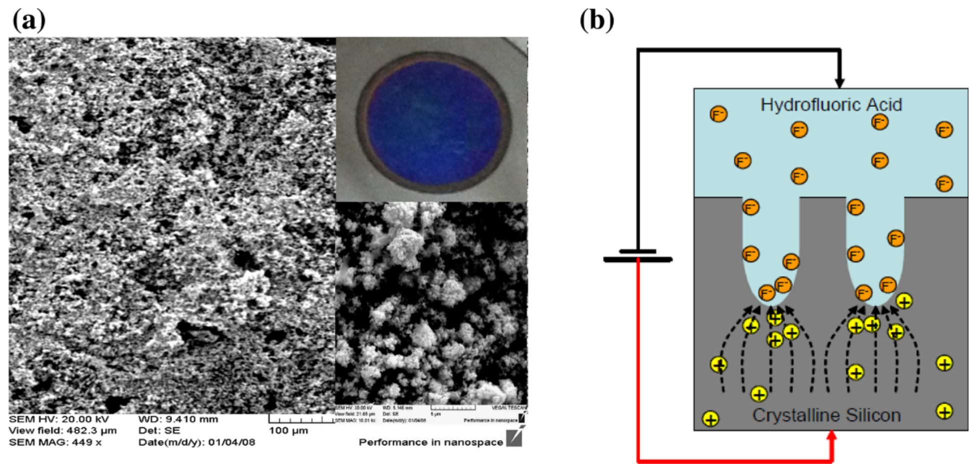

Fig. 12 SEM micrograph of PSi prepared with $J = 40$ mA/cm^2 at $t = 5$ min. **a** p-type porous silicon, and **b** schematic of PSi formation. Etching occurs only at the pore tips where the holes (h^+) are focused by the electric field

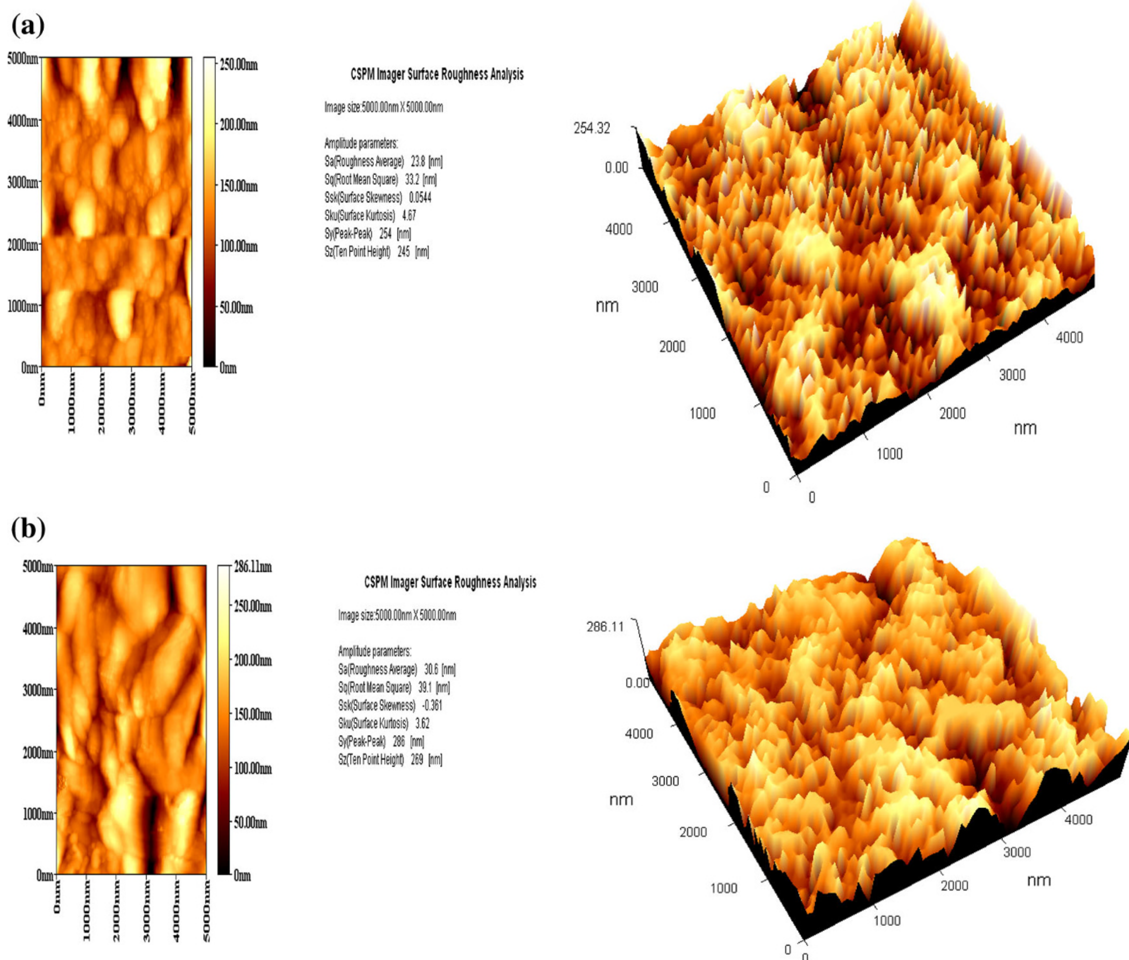

Fig. 13 Surface morphology of **a** deposited tin thin film (Sn)/p-PSi/c-Si and Au/n-SnO_2/p-PSi/c-Si oxidized at 600 °C

sharp and high-intensity diffracted peak noticed at $2\theta = 28.3212$ corresponds to (111) plane. This peak can be indexed as single crystal silicon cubic phase. The lattice constant of silicon is calculated and found 0.5364 nm which is very close to powder ASTM data (0.54 nm). The FWHM value of the diffracted silicon peak is 0.16960. XRD studies of porous silicon show distinct variations between the fresh silicon surface and the porous silicon surfaces formed at 40 mA/cm^2 anodizing current density and 5 min anodizing time.

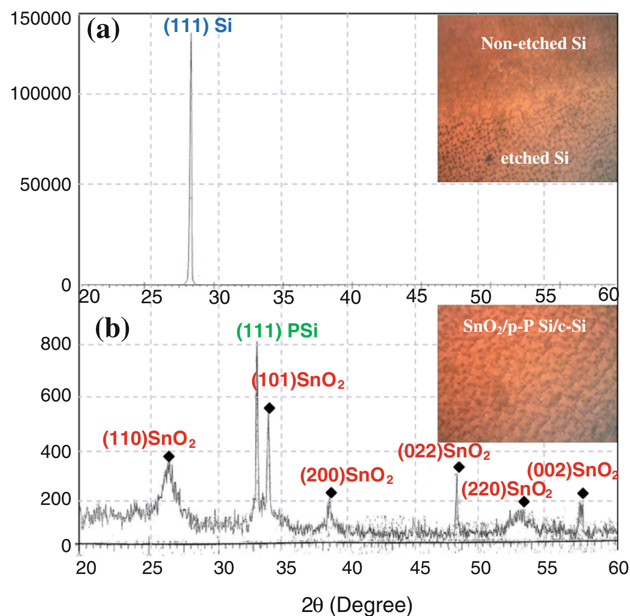

Fig. 14 X-Ray diffraction patterns for **a** silicon substrate, and **b** Au/n-SnO_2/p-PSi/c-Si

The XRD pattern of SnO_2 film deposited on porous silicon prepared at 40 mA/cm^2 is depicted in Fig. 14. Four diffracted peaks are observed at $2\theta = 26.657°$, 33.865°, 38.053°, 47.113°, 54.685° and 57.947°, corresponds to (110), (101), (200), (022), (220) and (002) planes. These peaks belong to polycrystalline SnO_2 film with tetragonal phase. The FWHMs of these four peaks are broader than that for SnO_2 film deposited on quartz substrate, while their intensities are smaller. During the growth of SnO_2 on PSi (here, nanocrystallites of Si), the SnO_2/Si interface has determined the favorable orientation for SnO_2: (110) or (101) or (200) or (022) or (220) and (002). This can be ascribed to the effect of lattice mismatch between Si and SnO_2, and also due to the effect of structural defects arising from porous structure that prevents high-crystalline SnO_2 film to grow.

The sensitivity, response and recovery characteristics of the sensor device have been studied by measuring the change in resistance, in the ambient and reducing gas atmosphere. The gas detection sensitivity (S) of the sensor device has been evaluated using the relation:

$$S = (R_a - R_g)/R_g \tag{7}$$

where R_a and R_g are resistance values of the sensor device in the ambient and reducing gas atmosphere, respectively. Variation of sensitivity as a function of response time is shown in Fig. 15. The maximum detection sensitivity of the sensor device toward H_2 and CO_2 gas is found to be 86 and 45 %, respectively. The figure depicts a short response time for H_2 and CO_2 gas, respectively, for reaching the maximum detection sensitivity indicated as above. The plot shows a non-exponential increase in sensitivity with response time and further indicates a saturation behavior in sensitivity for H_2 and CO_2 gas, respectively. The increase in sensitivity up to the saturation limit may be attributed to the raise in charge carrier density in the active surface, with the increase in time of gas exposure, due to rapid adsorption of gaseous species. This causes a fall in resistance, which consequently increases the sensitivity. On the other hand, saturation behavior of sensitivity, beyond the optimum response time (the time at which sensitivity reaches maximum), may be explained as follows: with the duration of exposure to gas, the gas interaction with the device active layer increases. After the culmination of optimum response time, the gas adsorption into the active layer reaches a saturation state causing the saturation of sensitivity.

Variation of detection sensitivity with the operating temperature is shown in Fig. 16. Sensitivity of the device increases with raise in operating temperature and reaches a maximum at 300 and 250 °C for H_2 and CO_2 gas, respectively. This may be attributed as follows: the rate of adsorption of the reducing gaseous species on to the active surface increases with the raise in operating temperature. This causes a rapid increase in the charge carriers and there

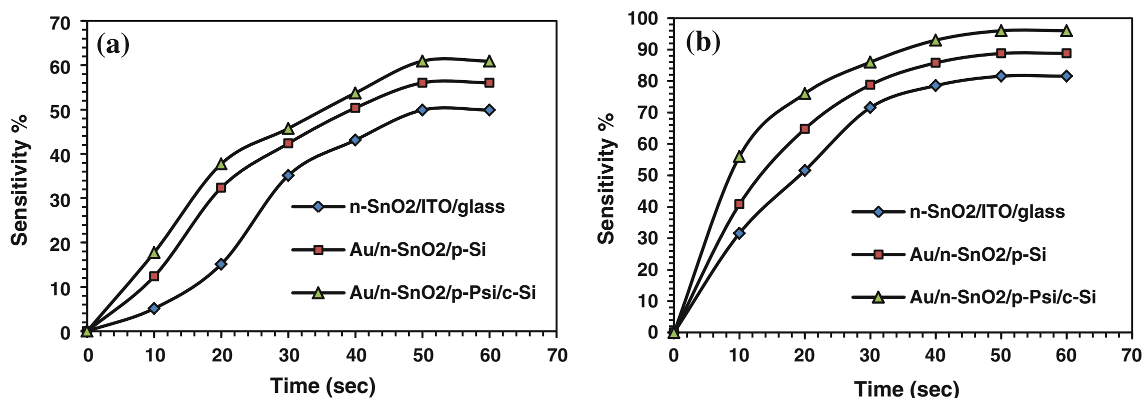

Fig. 15 Variation of sensitivity with time **a** CO_2 and **b** H_2

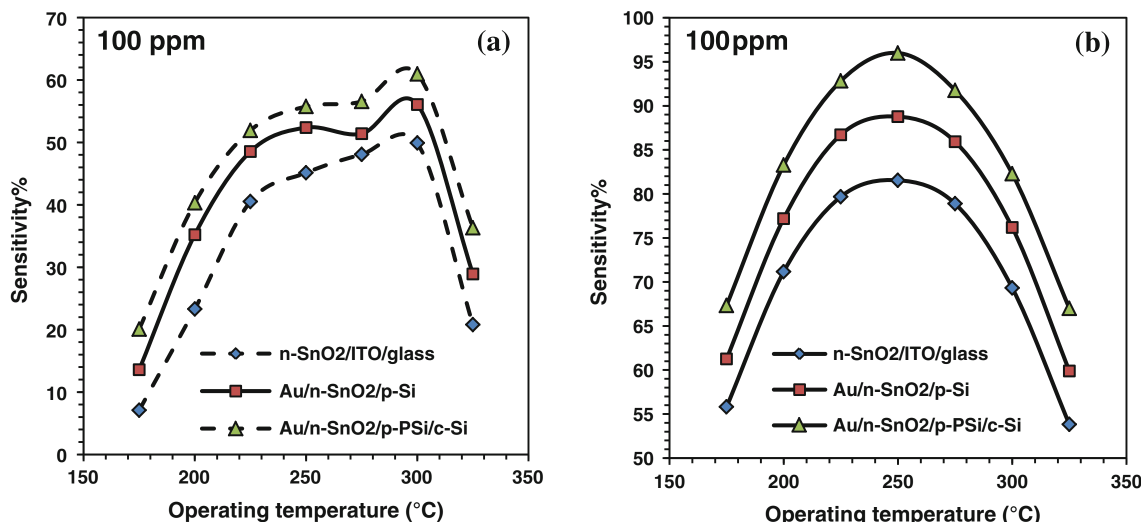

Fig. 16 Variation of sensitivity with operating temperature **a** CO_2 and **b** H_2

by resulting in a decrease in resistance and an increase in sensitivity. Further, the figure shows a fall in sensitivity beyond the optimum operating temperature, which may be attributed as follows: beyond the optimum operating temperatures, the structural deterioration effects dominates, which causes desorption of gaseous species from the active surface and this mechanism becomes more rapid, as the temperature is increased, resulting in the fall in sensitivity (Sankara and Vivek 2007).

Conclusions

Transparent and conducting SnO_2 thin film has been produced on (quartz, ITO, silicon and porous silicon) substrates using rapid photothermal oxidation of pure Sn in air at 600 °C oxidation temperature and different oxidation time. The structural, optical, electrical properties, scan electron microscope and atomic force microscope of the prepared films were studied. The transmittance T in the visible and NIR was investigated; the allowed direct energy gap was determined to be 3.18 eV at optimum condition of 600 °C and 90 s. The dependence of the resistivity on the film thickness and oxidation time has been studied. The optimum thickness of high transmittance and lowest resistivity is about 150 nm for SnO_2 were $\rho = 1.7 \times 10^{-3}$ Ω cm and $T = 88$ %. The sensitivity behaviors of the n-SnO_2/p-PSi/c-Si-based gas sensor to H_2 and CO_2 gas were investigated.

Open Access This article is distributed under the terms of the Creative Commons Attribution License which permits any use, distribution, and reproduction in any medium, provided the original author(s) and the source are credited.

References

Al-Hardan N, Abdulllah M (2009) The gas response enhancement from ZnO film for H2 gas detection. Appl Surf Sci 255:7749–7

Baik NS, Sakai G, Miura N, Yamazoe N (2000) Hydrothermally treated sol solution of tin oxide for thin film gas sensor. Sens Actuat B 63:74–79

Berger S, Quoizla S, Fave A, Ouldabbes A, Kaminski A, Perichon S, Sari NE, Barbier D, Laugier A (2001) Cryst Res Technol 36:1005

Bisi O, Ossicini S, Pavesi L (2000) Surf Sci Reports 38:1

Brown JR, Haycock PW, Smith LM, Jones AC, Williams EW (2000) Response behavior of tin oxide thin film gas sensors grown by MOCVD. Sens Actuat B 63(1):109–114

Carbajal GF, Tiburcio AS, Sanchez JM (2000) Thin film tin oxide-based propane gas sensors. Thin Solid Films 373(1–2):141–144

Cha KH, Park HC, Kim KH (1994) Effect of palladium doping and film thickness on the H_2-gas sensing characteristics of SnO_2. Sens Actuat B 21:91–96

Chaudhary VA, Mulla IS, Vijayamohanan K (1998) Comparative studies of doped and surface modified tin oxide towards hydrogen sensing: synergistic effects of Pd and Ru. Sens Actuat B 50:45–51

Chaudhary VA, Mulla IS, Vijayamohanan K (1999) Selective hydrogen sensing properties of surface functionalized tin oxide. Sens Actuat B 55:154–160

Choe Y-S, Chung J-H, Kim D-S, Kim G-H, Baik HK (1999) Phase transformation and morphological evolution of ion-beam sputtered tin oxide films on silicon substrate. Mater Res Bull 34(9):1473–1479

Choi WK, Song SK, Cho JS, Yoon YS, Choi D, Jung H-J, Koh SK (1997) H_2 gas-sensing characteristics of SnO_x sensors fabricated by a reactive ion-assisted deposition with/without an activation layer. Sens Actuat B 40:21–27

Devi GS, Masthan SK, Shakuntalav M, Rao J (1999) Correlation between structural properties and gas sensing characteristics of SnO_2 based gas sensors, J Mater Sci Mater Electron 10:545–549

Gaburro Z, Bellutti P, Chierchia R, Mulloni V, Pavesi L (2000) Mater Sci Eng B 69–70:109

Gordillo G, Moreno LC, De La Cruz W, Teheran P (1994) Preparation and characterization of SnO_2 thin films deposited

by spray pyrolysis from $SnCl_2$ and SnC_{l4} precursors. Thin Solid Films 252(1): 61–66
Gyogy E, Axente E (2000) Doped thin metal oxide films for catalytic gas sensors. Appl Surf Sci 2030:4123
Jayaraman V, Gnanasekar KI, Prabhu E, Gnanasekaran T, Periaswami G (1999) Sens Actuat B 55:147–153
Katsuki A, Fukui K (1998) H_2 selective gas sensor based on SnO_2. Sens Actuat B 52:30–37
Klein L (1988) Sol–gel technology for thin films, fibers, preforms, electronics, and specialty shapes. Part II. Noyes, Park Ridges
Kocka J, Fejfar A, Pelant I (1995) Phys Stat Solidi B 190:27
Kuku Titilayo A (1986) Physical properties of thin SnO_2 and SnO_2: Sb films obtained by a photolytic method. Thin Solid Films 142:241–250
Malyshev VV, Vasiliev AA, Eryshkin AV, Koltypin EA, Shubin YI, Buturlin AI, Zaikin VA, Chakhunashvili GB (1992) Gas sensitivity of SnO2 and ZnO thin-film resistive sensors to hydrocarbons, carbon monoxide and hydrogen. Sens Actuat B 10:11–14
Michel H-J, Leiste H, Schierbaum KD, Halbritter J (1998) Adsorbates and their effects on gas sensing properties of sputtered SnO_2 films. Appl Surf Sci 126:57–64
Mishra VN, Agarwal RP (1994) Thick-film hydrogen sensor. Sens Actuat B 21:209–212
Mitchell BS (2004) An introduction to materials engineering and science for chemical and materials engineers. John Wily & Sons, Inc., Hoboken. All rights reserved. Published simultaneously in Canada, p 43
Mohammed Khalid K (2005) The electrical and optical properties of SnO2 – Si (n) structure solar cells. Al-Rafidain Eng 13(3)
Mosadegh Sedghi S, Vesali Naseh M (2009) Sonochemically prepared SnO_2 quantum dots as a selective and low temperature Co sensor. Proceedings of World Academy of Science, Engineering and Technology 37(2070–3740)
Niranjan RS, Sainkar SR, Vijayamohanan K, Mulla IS (2002) Ruthenium: tin oxide thin film as a highly selective hydrocarbon sensor. Sens Actuat B 82(1):82–88
Park S-S, Mackenzie JD (1996) Thickness and microstructure effects on alcohol sensing of tin oxide thin films. Thin Solid Films 274:154–159
Pascual A, Fernandez JF, Sanchez CR (2002) J Appl Phys 92:866
Raviendra D, Sharma JK (1985) Electroless deposition of SnO_2 and antimony doped SnO_2 films. J Phys Chem Solids 46:945–950
Roman LS (2006) Optical band-edge absorption of oxide compound SnO_2. Appl Surf Sci 252:5361–5364
Sakai G, Baik NS, Miura N, Yamazoe N (2001) Gas sensing properties of tin oxide thin films fabricated from hydrothermally treated nanoparticles. Sens Actuat B 77:116–121
Sankara N, Vivek R (2007) Investigations on Pd: SnO_2/porous silicon structures for sensing LPG and NO_2 gas. Ionics 13:323–328
Sberveglieri G, Faglia G, Groppelli S, Nelli P (1992) Methods for the preparation of NO, NO_2 and H_2 sensors based on tin oxide thin films, grown by means of the r.f. magnetron sputtering technique. Sens Actuat B 8:79–88
Seal S, Shukla S (2002) Nanocrystalline SnO gas sensors in view of surface reactions and modifications. JOM 54(9):35–38, 60
Shimizu Y, Nakamura Y, Egashira M (1993) Effects of diffusivity of hydrogen and oxygen through pores of thick film SnO_2 based on their sensors properties. Sens Actuat B 13–14:128–131
Song S-K, Cho J-S, Choi W-K, Jung H-J, Choi D, Lee J-Y, Baik H-K, Koh S-K (1998) Structure and gas-sensing characteristics of undoped tin oxide thin films by ion-assisted deposition. Sens Actuat B 46:42–49
Van T, Dinh L (1998) Changes in the electronic properties of silicon nanocrystals as a function of particle size. Phys Rev Lett 80(17):27
Yadav JB, Patil RB, Puri RK, Vijaya Puri (2007) Studies on undoped SnO_2 thin film deposited by chemical reactive evaporation method. Mater Sci Eng 139(1):69–73
Yoshiaki S, Hiroharu K, Keitaro I, Tamiko O (2003) Preparation of tin oxide (SnO_2) thin film gas sensor by PLD method. Sci Links Jpn 123(2):222–227
Zhang B, Tian Y (2011a) Structural, optical, electrical properties and FTIR studies of fluorine doped SnO_2 films deposited by spray pyrolysis. J Mater Sci 46:1884–1889
Zhang B, Tian Y (2011b) The FTIR studies of SnO_2:Sb films deposited by spray pyrolysis. Mater Lett 65:1204–1206
Zhu H, Yao K (2006) A simple hydrothermal route for synthesizing SnO_2 quantum dots. Nanotechnology 17:2386–2389